Check for updates

NANO · MICRO small
www.small-journal.com

Spin-Flip Raman Scattering on Electrons and Holes in Two-Dimensional $(PEA)_2PbI_4$ Perovskites

Carolin Harkort, Dennis Kudlacik, Natalia E. Kopteva, Dmitri R. Yakovlev, Marek Karzel, Erik Kirstein, Oleh Hordiichuk, Maksym V. Kovalenko, and Manfred Bayer*

The class of Ruddlesden–Popper type $(PEA)_2PbI_4$ perovskites comprises 2D structures whose optical properties are determined by excitons with a large binding energy of about 260 meV. It complements the family of other 2D semiconductor materials by having the band structure typical for lead halide perovskites, that can be considered as inverted compared to conventional III–V and II–VI semiconductors. Accordingly, novel spin phenomena can be expected for them. Spin-flip Raman scattering is used here to measure the Zeeman splitting of electrons and holes in a magnetic field up to 10 T. From the recorded data, the electron and hole Landé factors (*g*-factors) are evaluated, their signs are determined, and their anisotropies are measured. The electron *g*-factor value changes from +2.11 out-of-plane to +2.50 in-plane, while the hole *g*-factor ranges between −0.13 and −0.51. The spin flips of the resident carriers are arranged via their interaction with photogenerated excitons. Also the double spin-flip process, where a resident electron and a resident hole interact with the same exciton, is observed showing a cumulative Raman shift. Dynamic nuclear spin polarization induced by spin-polarized holes is detected in corresponding changes of the hole Zeeman splitting. An Overhauser field of the polarized nuclei acting on the holes as large as 0.6 T can be achieved.

1. Introduction

Lead halide perovskite semiconductors attract nowadays great attention due to their remarkable potential for photonic applications.[1–4] They are available as bulk- and nanocrystals and also as 2D layered materials. 2D perovskites feature exceptional optical and electrical properties. By changing the thickness of the semiconductor layers and varying the organic barriers, their band gap energy changes from the infrared up to the ultraviolet spectral range.[5–7] The 2D perovskites exhibit robust environmental stability,[8] which makes them promising for optoelectronic[4,8,9] and photovoltaic[10–12] applications. The strong quantum confinement of electrons and holes results in excitons with large binding energies, which are additionally increased by dielectric confinement, approaching 200–500 meV.[13,14] The optical properties of 2D perovskites are therefore determined by exciton absorption and emission even in ambient conditions,[15,16] similar to 2D semiconductors like transition metal dichalcogenides.[17]

The band gap in lead halide perovskites is located at the R-point of the Brillouin zone for cubic crystal lattice and at the Γ-point for tetragonal or orthorhombic lattices.[18,19] In all these cases, the states at the bottom of the conduction band and the top of the valence band have spin 1/2. The perovskites band structure is inverted compared to conventional III–V and II–VI semiconductors, that is, in the vicinity of the band gap the valence band is mostly formed by the s-orbitals of Pb, while the conduction band states are contributed by the p-orbitals of Pb. As a result, the spin-orbit interaction modifies mostly the valence band states (and thus the hole effective mass and *g*-factor),[20–22] and the hyperfine interaction with the nuclear spins is much stronger for the holes than for the electrons, in contrast to conventional semiconductors.[21] Therefore, lead halide perovskites of different dimensionalities are considered as novel model systems for spin physics, offering interesting perspectives for spintronic and quantum information applications.[23]

The exciton structure in 2D perovskites was analyzed in ref. [24] for $(C_4H_9NH_3)_2PbBr_4$. The lowest exciton state splits into three fine structure levels (Γ_1^-, Γ_2^-, and Γ_5^-) as a result of the

C. Harkort, D. Kudlacik, N. E. Kopteva, D. R. Yakovlev, M. Karzel, E. Kirstein, M. Bayer
Experimentelle Physik 2
Technische Universität Dortmund
D-44227 Dortmund, Germany
E-mail: dmitri.yakovlev@tu-dortmund.de

O. Hordiichuk, M. V. Kovalenko
Laboratory of Inorganic Chemistry
Department of Chemistry and Applied Biosciences
ETH Zürich
CH-8093 Zürich, Switzerland

O. Hordiichuk, M. V. Kovalenko
Laboratory for Thin Films and Photovoltaics
Empa-Swiss Federal Laboratories for Materials Science and Technology
CH-8600 Dübendorf, Switzerland

The ORCID identification number(s) for the author(s) of this article can be found under https://doi.org/10.1002/smll.202300988.

© 2023 The Authors. Small published by Wiley-VCH GmbH. This is an open access article under the terms of the Creative Commons Attribution-NonCommercial-NoDerivs License, which permits use and distribution in any medium, provided the original work is properly cited, the use is non-commercial and no modifications or adaptations are made.

DOI: 10.1002/smll.202300988

exchange interaction. Among them the Γ_1^- state with the z-component of the total angular momentum $J_z = 0$, which is the lowest energy state, is dark. The higher energy state $\Gamma_2^-(J_z = 0)$ is only optically active for the photon electric field parallel to *c*-axis ($\mathbf{E}\|c$), that is, it cannot be excited by the light with *k*-vector parallel to *c*-axis. The twofold spin degenerated $\Gamma_5^-(J_z = \pm 1)$ state is optically active in $\mathbf{E}\perp c$ configuration and is bright. It was shown experimentally that in $(C_4H_9NH_3)_2PbBr_4$ the oscillator strength of the Γ_5^- state is 800 times larger compared to the one of the Γ_2^- state.[25] Recently, the exciton fine structure in $CsPbBr_3$ 2D nanoplatelets of various thicknesses was considered in ref. [26], where the Γ_5^- states were denoted as (*X*, *Y*) states and the Γ_2^- state as a *Z* state.

Recent studies show that a similar level of optical spin control can be achieved in perovskites as in conventional semiconductors. To that end, the optical and magneto-optical techniques established for studying spin-dependent phenomena were tested with respect to their suitability for lead halide perovskites: optical orientation,[27–30] optical alignment,[28] polarized emission in magnetic field,[31–33] time-resolved Faraday/Kerr rotation[21,34,35] and spin-flip Raman scattering[22,25] were demonstrated. Some of them were also used to study spin properties including their dynamics in 2D perovskites. Application of high magnetic fields up to 60 T provided information on the exciton fine structure and exciton Landé factor (*g*-factor).[24,36–42] The exciton spin dynamics down to subpicosecond time scales were addressed by optical spin orientation measured by time-resolved transmission.[43–47] Most of the dynamical studies were carried out above liquid nitrogen up to room temperature, where the spin relaxation times do not exceed a few picoseconds. Recently, time-resolved Kerr rotation allowed measurements of the coherent dynamics of electron spins in the $(PEA)_2PbI_4$ 2D perovskite.[48] In these experiments, longitudinal spin relaxation times up to 25 µs were found at the temperature of 1.6 K. In addition, the electron *g*-factor was measured, showing a considerable anisotropy. At present, the experimental information on the electron and hole *g*-factors in 2D perovskites, being the key parameters for understanding and interpreting spin-dependent phenomena, is still limited, and we are also not aware of corresponding theoretical considerations.

Spin-flip Raman scattering (SFRS) spectroscopy is another powerful magneto-optical technique in spin physics, providing direct information on the Zeeman splitting of electrons, holes, and excitons, and on the optical selection rules due to the spin level structure of exciton complexes, determined by their symmetries and exciton-carrier spin interactions.[49–55] SFRS signals are strongly enhanced when the laser photon energy is tuned into resonance with the exciton. SFRS measurements are experimentally challenging due to the close spectral proximity of the spin-flip signals and the laser line, as the spin-flip Raman shift is on the order of a few hundred µeV. Recently, however, the feasibility of SFRS for measuring the electron and hole *g*-factors in $CsPbBr_3$ and $MAPbI_3$ lead halide perovskite crystals was demonstrated.[22]

In this paper, we report on an SFRS study of the electron and hole *g*-factors in Ruddlesden–Popper type $(PEA)_2PbI_4$ 2D perovskites. The experiments are performed at cryogenic temperatures in magnetic fields up to 10 T, applied in different geometries in order to measure the *g*-factor anisotropy. The spin-flip signals originate from resident electrons and holes interacting with photogenerated excitons. Further, nuclear spin polarization by spin polarized holes is evidenced through corresponding shifts of the hole spin-flip line.

2. Experimental Results

2.1. Optical Properties of 2D Perovskites $(PEA)_2PbI_4$

We study the 2D Ruddlesden–Popper type perovskite structure $(PEA)_2PbI_4$, which consists of a corner-shared network of PbI_6-octahedral monolayers constituting quantum wells separated by van der Waals-bonded pairs of PEA (phenethylammonium) molecules. Due to the strong quantum confinement of electrons and holes in the 2D perovskite layers, the band gap energy increases to 2.608 eV at $T = 2$ K.[38] The reduced dimensionality and the dielectric confinement effect,[19] provided by the difference of dielectric constants between the perovskite and the PEA, strongly increase the exciton binding energy in $(PEA)_2PbI_4$ to 260 meV,[38,42] in comparison to 16 meV in bulk $MAPbI_3$.[56]

The pronounced exciton resonance in $(PEA)_2PbI_4$ is seen in the reflectivity (R) spectrum, measured at the temperature of $T = 1.6$ K, see **Figure 1**a. The resonance line with the minimum at 2.341 eV and the full width at half maximum of 6.6 meV originates from the free exciton. In external magnetic field applied in the Faraday geometry ($\mathbf{B}_F\|\mathbf{k}\|c$), the exciton spin states +1 and –1 detected in σ^+ and σ^- circular polarization, respectively, are subject to Zeeman splitting by $E_{Z,X} = g_{X,c}\mu_B B_F$. Here, the *c*-axis is perpendicular to the 2D planes, $\mathbf{k}$ is the light wave vector, $g_{X,c}$ is the exciton *g*-factor along the *c*-axis, and μ_B is the Bohr magneton. Reflectivity spectra at $B_F = 7$ T measured in σ^+ and σ^- polarization are shown in Figure 1b. The different energies of the exciton resonance in the two spectra reflect the Zeeman splitting. In Figure 1c we present the magnetic field dependence of the exciton Zeeman splitting, from its linear fit the exciton *g*-factor $g_{X,c} = +1.6 \pm 0.1$ is evaluated. Note that in this experiment the *g*-factor sign can be determined: a positive value corresponds to a high energy shift of the σ^+ polarized resonance relative to the σ^- polarized one.

The photoluminescence (PL) spectrum shows a strong emission line with the maximum at 2.343 eV and the full width at half maximum of about 10 meV, see Figure 1a. The PL line coincides in energy with the free exciton resonance measured in reflectivity. However, note that the PL line is broader than the reflectivity line. It is plausible to assign the line to the exciton emission of both free and weakly localized excitons. This assignment is supported by time-integrated and time-resolved spectroscopic studies at cryogenic temperatures reported in refs. [39,40,57–59], showing that the PL band is composed of at least two emission lines. Their recombination dynamics show times in the range of 300 ps to 10 ns, highlighting the free- and bound-exciton origin.

For the studied $(PEA)_2PbI_4$, the population dynamics are measured by time-resolved differential reflectivity for resonant excitation of the exciton. The results are reported in ref. [48]. The dynamics trace reveals decays with times of 20 and 340 ps. Also a longer-lived component with a decay exceeding 1 ns is

© 2023 The Authors. Small published by Wiley-VCH GmbH

16136829, 2023, 32, Downloaded from https://onlinelibrary.wiley.com/doi/10.1002/smll.202300988 by Technische Universitaet Dortmund, Wiley Online Library on [07/02/2025]. See the Terms and Conditions (https://onlinelibrary.wiley.com/terms-and-conditions) on Wiley Online Library for rules of use; OA articles are governed by the applicable Creative Commons License

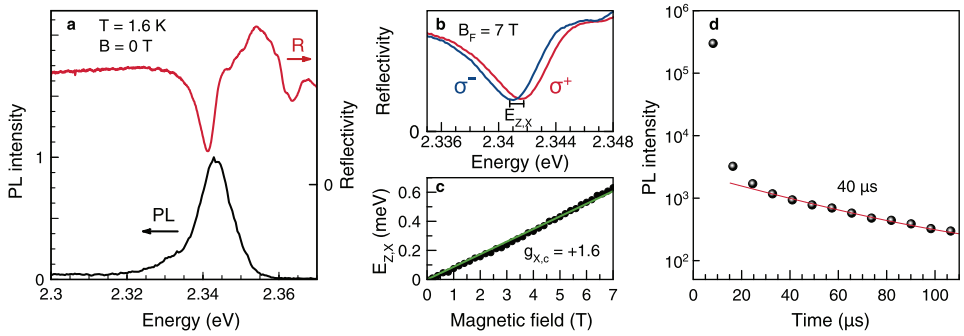

Figure 1. Optical properties of excitons in $(PEA)_2PbI_4$ at $T = 1.6$ K. a) Reflectivity (red) and photoluminescence (black) spectra. The PL is excited at 2.412 eV photon energy using $P = 10.8$ W cm^{-2} excitation power. b) Counter-circularly polarized reflectivity spectra measured in Faraday geometry at $B_F = 7$ T ($\mathbf{B}_F \| \mathbf{k} \| c$). The exciton Zeeman splitting of $E_{Z,X} = 0.63$ meV can be determined with good accuracy. c) Magnetic field dependence of the exciton Zeeman splitting evaluated from magneto-reflectivity data (symbols). The green line is a B-linear fit. d) PL dynamics (symbols) measured at the PL maximum of 2.343 eV. Pulsed excitation is used at an energy of 3.493 eV photon energy with an average power of $P = 3$ W cm^{-2}. The line is an exponential fit of the decay at longer time with the time constant of 40 μs.

observed. We attribute the short dynamics of 20 ps to the lifetime of the bright excitons with a large oscillator strength in 2D perovskites. The lifetime is given by their radiative recombination and their relaxation into dark exciton states. This interpretation is in agreement with literature data on the low temperature recombination dynamics in $(PEA)_2PbI_4$.[58–60] The slower 340 ps dynamics can be attributed to non-geminate recombination of charge carriers.

In Figure 1d, the PL dynamics measured at the maximum of the PL line across a much longer temporal range up to 100 μs are shown. Recombination processes with a decay time of about 40 μs are observed, which greatly exceeds the typical times in exciton dynamics. This evidences that long-living resident carriers are present in the studied structures. These resident carriers can be photo-generated electrons and holes which are localized at spatially separated sites. We will term them as resident electrons and holes and will show that they give the main contribution to the measured SFRS signals. Note that the existence of resident carriers is typical for lead halide perovskites, as we showed for bulk $CsPbBr_3$,[35] $FA_{0.9}Cs_{0.1}PbI_{2.8}Br_{0.2}$,[21] and $MAPbI_3$[61] crystals using optical techniques.

The line forming a shoulder of the PL line at 2.330 eV, see Figure 1a, was assigned in literature either to dark exciton emission[26,39,57,62] or to phonon-assisted bright exciton recombination.[58]

2.2. Spin-Flip Raman Scattering in Close-to-Faraday Geometry

We apply spin-flip Raman scattering to study the properties of the resident carrier spins in the 2D $(PEA)_2PbI_4$ perovskite. In an external magnetic field, **B**, the spin sublevels of the electrons (e) and the holes (h) are split by the Zeeman energy $E_{Z,e(h)} = g_{e(h)}\mu_B B$, which is proportional to the magnetic field strength and the electron (hole) g-factor $g_{e(h)}$. In the process of Raman light scattering, the carrier spin can flip changing its orientation, which requires either absorption or dissipation of the energy amount equal to $E_{Z,e(h)}$, depending on whether the spin flips from the lower to the upper energy level or vice versa. Therefore, the energy of the scattered photon differs from the laser photon energy by $E_{Z,\,e(h)}$. In case of energy absorption, the Raman shift occurs to lower energies (Stokes shift), note, however, that in SFRS experiments it is common to refer to this case as positive Raman shift. In case of energy dissipation, the shift is to larger energies (anti-Stokes shift), so that the Raman shift values are negative. For light scattering in semiconductors, an exciton serves as a mediator between light and spins,[52,53] because the light–matter interaction is greatly enhanced at the exciton resonance.

The schematics of the applied experimental geometries are shown in **Figure 2**a. In the Faraday geometry the magnetic field is parallel to the light k-vector ($\mathbf{B}_F \| \mathbf{k}$), which in turn is parallel to the crystal c-axis ($\mathbf{k} \| c$). In the studied $(PEA)_2PbI_4$, SFRS signal is absent in the pure Faraday geometry, because the carrier spin states +1/2 and −1/2 are not mixed by magnetic field and, thus, the spin-flip process is suppressed. Such mixing already occurs for small tilt angles, for example, at $\theta = 10°$, and then indeed SFRS signals become pronounced. We refer to this geometry as "close-to-Faraday geometry," where the Zeeman splitting is dominated by the g-factor component along the c-axis ($g_{e(h),c}$). The SFRS spectrum measured at $B = 9.4$ T with the excitation laser tuned to the exciton resonance at 2.345 eV, is shown in Figure 2b. The spin-flip lines are more pronounced in the anti-Stokes spectral range, as there the contribution of background photoluminescence is minimized.

Four spin-flip lines in the SFRS spectrum labeled by E_h, E_{e+h}, E_e, and E_{e-h} are seen in Figure 2b. They are absent at zero magnetic field, as expected from the vanishing Zeeman splitting so that the spin-flip lines coincide with the exciting laser energy. With increasing magnetic field the lines shift linearly from the laser energy (referred to as zero). The details of their shifts are shown in **Figure 3**a–c. The E_h line is only detected in high magnetic fields (see the black circles in Figure 3c) due to its small shift amounting to only −0.078 meV at 9.4 T, which is associated with the spin-flip of the hole having $|g_{h,\,c}| = 0.13$. The electron spin-flip line shows a much larger shift of $E_e = -1.137$ meV at $B = 9.4$ T. Its magnetic field dependence in Figure 3a allows us to evaluate $|g_{e,c}| = 2.11$, agreeing well with $g_{e,c} = +2.05 \pm 0.05$ determined from time-resolved Kerr rotation on the same sample.[48]

© 2023 The Authors. Small published by Wiley-VCH GmbH

16136829, 2023, 32, Downloaded from https://onlinelibrary.wiley.com/doi/10.1002/smll.202300988 by Technische Universitaet Dortmund, Wiley Online Library on [07/02/2025]. See the Terms and Conditions (https://onlinelibrary.wiley.com/terms-and-conditions) on Wiley Online Library for rules of use; OA articles are governed by the applicable Creative Commons License

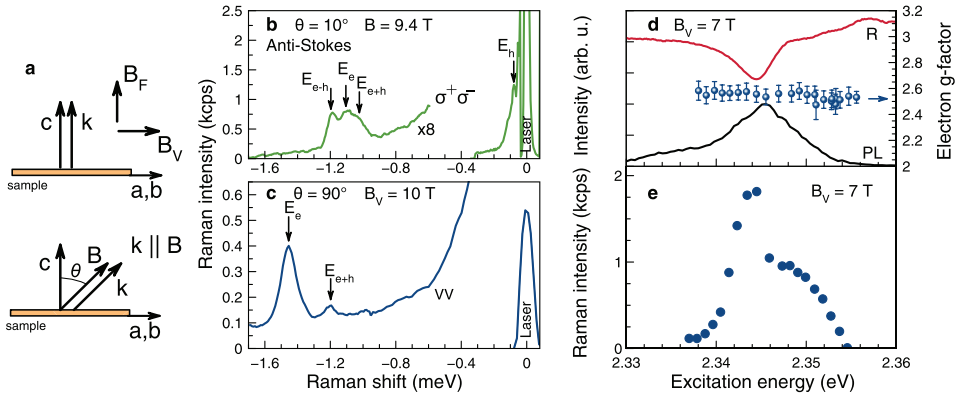

Figure 2. Spin-flip Raman scattering in $(PEA)_2PbI_4$. a) Sketch of the experimental geometry. Upper diagram is for the Faraday ($\mathbf{B}_F \| c$) and Voigt ($\mathbf{B}_V \| (a, b)$) geometry with the laser light vector $\mathbf{k} \| c$. Bottom diagram is for the tilted field geometry. The angle θ specifies the tilt between $\mathbf{B}$ and the c-axis ($\mathbf{k} \| \mathbf{B}$). b) SFRS spectrum in the anti-Stokes spectral range (negative Raman shift) for $\theta = 10°$, measured for $E_{exc} = 2.345$ eV laser photon energy with the power $P = 5.7$ W cm^{-2}. The spectrum is multiplied by a factor of 8. The shifts of the hole E_h, the electron E_e, and their double flip (E_{e+h} and E_{e-h}) lines are marked with arrows. c) SFRS spectrum in Voigt geometry at $B_V = 10$ T using linearly co-polarized excitation and detection. d) Reflectivity and photoluminescence spectra at $B_V = 7$ T. Electron g-factor dependence on the excitation energy (circles). e) SFRS intensity resonance profile for the electron spin-flip at $B_V = 7$ T. All data are measured at $T = 1.6$ K.

Identification of the hole and electron SFRS lines is done by comparing their g-factors with the universal dependence of the carrier g-factors on the band gap energy, that has recently been established for bulk lead halide perovskites.[22] According to this dependence for materials with band gap energies around 2.3 eV, g-factor values of $g_e \approx +2.0$ and $g_h \approx +0.7$ are predicted. We expect some, but not drastic deviations from this dependence for the 2D perovskites. Therefore, we assign the spin-flip line with the larger shift to the resident electron with positive sign of the g-factor.

Another approach to distinguish electrons from holes is based on their interactions with the nuclear spin system, since in lead halide perovskites the hole–nuclei interaction is about five times stronger than the electron-nuclei one.[21] This also leads to a much stronger dynamic nuclear polarization (DNP) by the holes. In Section 2.6 we show that DNP can be detected with the SFRS technique and that its effect is considerable for the E_h line. Note that it is absent for the E_e line, in accordance with our assignment. From this experiment, the sign of the hole g-factor can be unambiguously determined. For the studied $(PEA)_2PbI_4$, the hole g-factor is negative, that is, $g_{h,c} = -0.13$.

The electron line E_e has two satellites, $E_{e\text{-}h}$ and E_{e+h}, which are shifted by the hole Zeeman splitting. The slopes in their magnetic field dependence give $|g_{e\text{-}h,c}| = 2.25$ and $|g_{e+h,c}| = 1.94$, see Figure 3b. These lines are provided by double spin-flip processes, in which simultaneously electron and hole spin-flips are

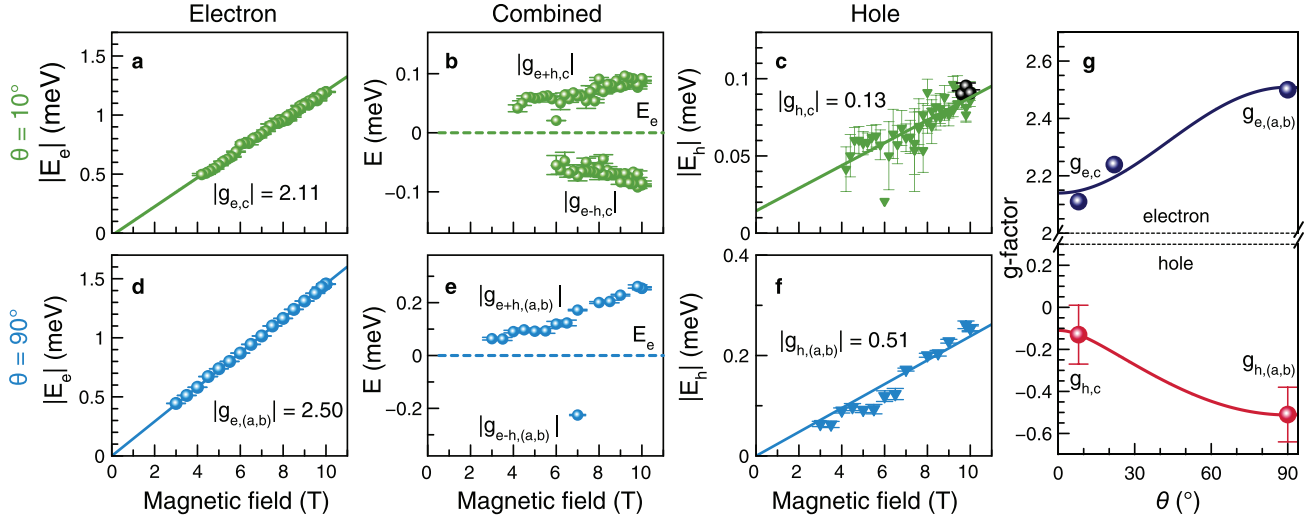

Figure 3. Raman shifts of the spin-flip lines in magnetic field and evaluated carrier g-factors in $(PEA)_2PbI_4$. Magnetic field dependences of the anti-Stokes SFRS shifts measured in the close-to-Faraday ($\theta = 10°$) and Voigt ($\theta = 90°$) geometries. a,d) Electron E_e shift. b,e) Double spin-flip E_{e+h} and E_{e-h} shifts after subtracting the shift of E_e. c,f) Hole E_h shift evaluated from the double spin-flip shifts (colored triangles). Black dots in panel (c) give direct measurements of the hole spin-flip shift of the E_h line. In all panels, B-linear fits are shown by the solid lines. g) g-factor anisotropy for the tilt angle θ tuned between Faraday and Voigt geometry. Lines are fits with Equation (1). All measurements presented here are performed at $T = 1.6$ K with $E_{exc} = 2.345$ eV laser photon energy using $P = 7.5$ W cm^{-2} excitation power.

© 2023 The Authors. Small published by Wiley-VCH GmbH

16136829, 2023, 32, Downloaded from https://onlinelibrary.wiley.com/doi/10.1002/smll.202300988 by Technische Universitaet Dortmund, Wiley Online Library on [07/02/2025]. See the Terms and Conditions (https://onlinelibrary.wiley.com/terms-and-conditions) on Wiley Online Library for rules of use; OA articles are governed by the applicable Creative Commons License

involved. This is a rather unusual SFRS process. Double electron spin-flip was found experimentally in 1972 for an exciton interacting with two donor-bound electrons in CdS,[63] later in ZnTe,[64] and recently for two localized electrons interacting with the same exciton in CdSe colloidal nanoplatelets.[55] The according theoretical consideration can be found in refs. [65–67]. The $E_{e\text{-}h}$ and E_{e+h} line shifts are much larger compared to the E_h line, and can therefore be resolved in a larger range of magnetic fields starting from 4 T. We use the difference between the double spin-flip line E_{e+h} and the electron line E_e to evaluate the hole Zeeman splitting versus magnetic field in Figure 3c. Note that the full width at half maximum, taken from the Gaussian fit of the electron spin-flip line, is about seven times larger (50 μeV) than that for the hole (7 μeV), which indicates a broader electron *g*-factor dispersion.

Commonly, SFRS signals have a pronounced polarization dependence, caused by the optical selection rules and the involved scattering mechanisms. The spectrum shown in Figure 2b is measured in a cross circularly-polarized configuration with σ^+ polarized excitation and σ^- polarized detection. The other polarization configurations are shown in Figure S1a, Supporting Information, for both the anti-Stokes and Stokes spectral ranges. Surprisingly, the polarization dependence is weak. Possible reasons for that are discussed in Section 2.7.

2.3. Spin-Flip Raman Scattering in Voigt Geometry

In order to determine the in-plane components of the electron and hole *g*-factors, we perform SFRS measurements in the Voigt geometry, where $\mathbf{B}_V \perp \mathbf{k}$, $\mathbf{B}_V \| (a, b)$ and $\theta = 90°$. In Figure 2c the SFRS spectrum for linearly co-polarized excitation and detection in the Voigt geometry at $B_V = 10$ T is shown. This geometry is favorable for SFRS experiments because the spin states are mixed by the perpendicular magnetic field, facilitating an efficient spin-flip process. The comparison of the SFRS spectra in Figures 2b and 2c shows that the SFRS intensity in the Voigt geometry is about five times higher than in the Faraday geometry. In the Voigt geometry the Raman shift of the electron E_e line corresponds to $|g_{e,(a,b)}| = 2.50$, see also Figure 3d. This value is in good agreement with $g_{e,\,(a,b)} = +2.45 \pm 0.05$ measured by time-resolved Kerr rotation.[48] The slope of the linear fit to the double spin-flip E_{e+h} Raman shift corresponds to $|g_{e+h,\,(a,b)}| = 1.98$, see Figure 3e. As the E_h line cannot be resolved in this geometry, we calculate its Raman shift from the shift difference between E_{e+h} and E_e. From the data in different magnetic fields we determine the hole *g*-factor $g_{h,(a,b)} = -0.51$ (Figure 3f). Note that the $E_{e\text{-}h}$ line cannot be well detected in Voigt geometry. The SFRS spectra are measured in different configurations of linear polarization, however, a noticeable influence of selection rules is not found, more information is provided in the Figure S1b, Supporting Information.

It is worth pointing out that the amplitude of the spin-flip lines is sensitive to temperature. We show in Figure S2, Supporting Information, that the electron SFRS line amplitude decreases for temperatures exceeding 5 K and becomes weak above 16 K. We suggest that thermal delocalization of the resident electrons is the mechanism that reduces the efficiency of the SFRS process. The estimated activation energy is about 2.1 meV.

2.4. Resonance Profile of Spin-Flip Raman Scattering

The SFRS intensity has a strong spectral dependence on the laser photon energy as shown in Figure 2e for the E_e line, measured in the Voigt geometry at $B_V = 7$ T. The maximum of the resonance profile coincides with the free exciton energy in the reflectivity spectrum shown in Figure 2d, where also the PL line is given for comparison. This highlights the key role of the exciton in the SFRS process. The exciton resonantly enhances the laser excitation and scattering through the interaction with resident carriers, whose spin-flip Raman shift is measured. Similar results were reported for CdTe/(Cd,Mg)Te quantum wells with a low density of resident electrons[53] and for singly-charged (In,Ga)As/GaAs quantum dots.[54] In Figure 2d, the electron *g*-factor is shown as function of the excitation energy. It remains constant across the investigated energy range.

2.5. *g*-Factors of Electrons and Holes and their Anisotropy

The electron and hole *g*-factors can be precisely determined from the Raman shifts of the respective lines at different magnetic fields. The results in the close-to-Faraday and Voigt geometries are presented in Figure 3. The electron *g*-factors are taken from the shift of the E_e line, see Figure 3a,d. Figure 3b,e illustrate the shifts of the double spin-flip lines E_{e+h} and $E_{e\text{-}h}$, which are plotted relative to the E_e line shift. The differences between the E_e and the double spin-flip line shifts correspond to the hole Zeeman splitting, shown in Figure 3c,f. Only in high magnetic fields the E_h shift can be directly measured. The corresponding values of the *g*-factors are given in the panels of Figure 3 and are also collected in **Table 1**, in which the signs of the *g*-factors are given.

The anisotropy of the carrier *g*-factors is inherent for 2D structures and originates from the reduced symmetry of the band structure. For the studied $(PEA)_2PbI_4$ sample the anisotropy is shown in Figure 3g, where the experimental data for the close-to-Faraday and Voigt geometries are complemented by measurements at the magnetic field tilt angle of $\theta = 22°$. The angular dependence of the *g*-factor can be described by

$$g(\theta) = \sqrt{(g_c \cos\theta)^2 + (g_{(a,b)} \sin\theta)^2} \quad (1)$$

Table 1. Overview of the *g*-factors in the close-to-Faraday geometry ($\theta = 10°$) and in the Voigt geometry ($\theta = 90°$) for $(PEA)_2PbI_4$ measured by SFRS and time-resolved Kerr rotation.[48] The measurement accuracy is ±0.05 in all cases. The exciton Zeeman splitting measured by magneto-reflectivity in Faraday geometry gives $g_{X,\,c} = +1.6 \pm 0.1$.

	Close to Faraday geometry, $\theta = 10°$				Voigt geometry, $\theta = 90°$			
	$g_{e,\,c}$	$g_{h,\,c}$	$g_{e\text{-}h,\,c}$	$g_{e+h,\,c}$	$g_{e,\,(a,b)}$	$g_{h,\,(a,b)}$	$g_{e\text{-}h,\,(a,b)}$	$g_{e+h,\,(a,b)}$
SFRS	+2.11	−0.13	+2.25	+1.94	+2.50	−0.51	+2.93	+1.98
TRKR[48]	+2.05				+2.45			

© 2023 The Authors. Small published by Wiley-VCH GmbH

16136829, 2023, 32, Downloaded from https://onlinelibrary.wiley.com/doi/10.1002/smll.202300988 by Technische Universitaet Dortmund, Wiley Online Library on [07/02/2025]. See the Terms and Conditions (https://onlinelibrary.wiley.com/terms-and-conditions) on Wiley Online Library for rules of use; OA articles are governed by the applicable Creative Commons License

The electron *g*-factor anisotropy measured by TRKR in a vector magnet with smaller steps of the tilt angle can be found in ref. [48]. It is interesting to note that the anisotropies of g_e and g_h almost compensate each other, so that their sum stays nearly isotropic, $g_{e,c} + g_{h,c} = +1.98$ and $g_{e,(a,b)} + g_{h,(a,b)} = +1.99$. A similar behavior was recently found for bulk $CsPbBr_3$ crystals.[22]

The *g*-factor of the bright exciton in lead halide perovskites is the sum of the carrier *g*-factors

$$g_X = g_e + g_h \quad (2)$$

Therefore, the exciton *g*-factor in 2D $(PEA)_2PbI_4$ should be nearly isotropic despite a clear crystal anisotropy. In fact, g_X may deviate from the relation (2), as some *g*-factor renormalization can occur at finite carrier *k*-vectors in the exciton. It is instructive to check this relation for $(PEA)_2PbI_4$. Here $g_{e,c} + g_{h,c} = +1.98$ can be compared with the $g_{X,c} = +1.6$ measured by magneto-reflectivity (Figure 1c). Indeed, the exciton *g*-factor is about 0.4 smaller than the sum. We attribute this difference to the large exciton binding energies in the 2D $(PEA)_2PbI_4$ perovskite. Further model calculations are needed to identify the involved mechanisms.

2.6. Dynamic Nuclear Polarization

The spin dynamics of electrons and holes in semiconductors are strongly influenced by their hyperfine interaction with the nuclear spin system.[68] In conventional III–V and II–VI semiconductors the conduction band electrons with s-type wave functions have stronger interaction with the nuclei spins compared to the valence band holes with p-type wave functions. This situation is reversed in lead halide perovskites, where the Pb ions greatly contribute to the states around the band gap.[21,61] Their p-orbitals form the conduction band, while the s-orbitals contribute to the valence band. As a result, the hyperfine interaction of the holes is about five times stronger than that of electrons. Similar properties are expected for $(PEA)_2PbI_4$.

The hyperfine interaction of carriers with the nuclei can be assessed by the effect of dynamic nuclear polarization (DNP). Spin polarized carriers, which can be generated by circularly polarized light using optical orientation, generate the Knight field ($\mathbf{B}_K$) that acts as an effective magnetic field on the nuclear spins. Thereby the carrier spin polarization can be transferred to the nuclear spin system, so that it becomes polarized. In turn, the polarized nuclear system induces the Overhauser field ($\mathbf{B}_N$) that acts on the carrier spins and changes their Zeeman splitting, see scheme in **Figure 4**d. Details of DNP model description are given in ref. [21]. Here for simplicity, we will consider only the hole contribution, as we found experimentally that in $(PEA)_2PbI_4$ the holes are dominant in polarizing the nuclear spins.

The spin polarization of optically oriented holes $\langle \mathbf{S}_h \rangle$ is transferred to the nuclei and induces the average nuclear spin polarization $\langle \mathbf{I} \rangle$ given by

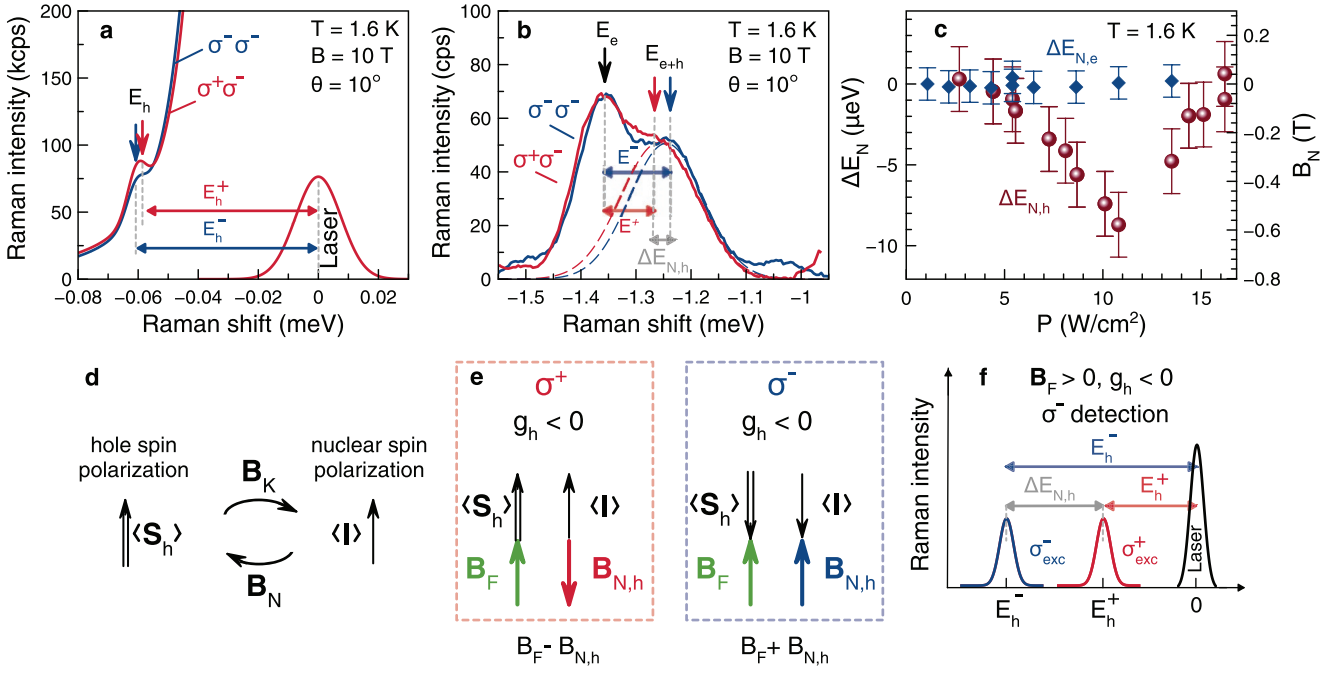

Figure 4. Dynamic nuclear polarization of holes detected via SFRS in $(PEA)_2PbI_4$. a) Raman shift of the hole E_h line measured in $\sigma^-\sigma^-$ and $\sigma^+\sigma^-$ polarization for $P = 5.1$ W cm^{-2} excitation power. b) Raman shift of the electron E_e and double spin-flip E_{e+h} lines measured in different polarizations for $P = 13.5$ W cm^{-2}. c) Power density dependences of the energy splitting $\Delta E_N = E^+ - E^-$ for the electron and hole shifts from panel (b). Right axis gives the corresponding Overhauser field B_N. d) Schematic illustration of the hyperfine interaction in a carrier-nuclei spin system. The effective Knight field (B_K) of the spin polarized holes $\langle \mathbf{S}_h \rangle$ acts on the nuclear spin system. The average nuclear spin polarization $\langle \mathbf{I} \rangle$ acts back via the Overhauser field ($B_{N,h}$) on the hole spin. e) $\mathbf{B}_{N,h}$ orientation scheme for $g_h < 0$ with σ^+ or σ^- excitation in an external magnetic field applied in the Faraday geometry. f) Schematic Raman spectrum highlighting the effect of DNP on the Raman shift. The difference between the Raman line shifts for σ^+ and σ^- excitation is proportional to $2B_{N,h}$.

© 2023 The Authors. Small published by Wiley-VCH GmbH

16136829, 2023, 32, Downloaded from https://onlinelibrary.wiley.com/doi/10.1002/smll.202300988 by Technische Universitaet Dortmund, Wiley Online Library on [07/02/2025]. See the Terms and Conditions (https://onlinelibrary.wiley.com/terms-and-conditions) on Wiley Online Library for rules of use; OA articles are governed by the applicable Creative Commons License

$$\langle \mathbf{I} \rangle = l \frac{4I(I+1)}{3} \frac{\mathbf{B}(\mathbf{B}\langle \mathbf{S}_h \rangle)}{B^2} \quad (3)$$

Here l is the leakage factor characterizing DNP losses due to relaxation processes and I is the nuclear spin. The nuclear spin polarization builds up along the direction of projection of $\langle \mathbf{S}_h \rangle$ onto the magnetic field, and therefore its direction can be controlled by the light helicity, which determines the $\langle \mathbf{S}_h \rangle$ orientation. The nuclear spin polarization can be converted into the Overhauser field

$$\mathbf{B}_{N,h} = \frac{\alpha A_h \langle \mathbf{I} \rangle}{g_h \mu_B} \quad (4)$$

with the positive hyperfine coupling constant for holes $A_h > 0$. Here α is abundance of nuclear isotopes with nonzero spin. The sign of $\mathbf{B}_{N,\,h}$ is determined by the sign of the hole g-factor, which offers an experimental tool for evaluating the g_h sign. In Figure 4e, diagrams for the orientation possibilities of the magnetic and effective fields as well as the spin polarization are given for σ^+ and σ^- circular polarized excitation. Here, we take $g_h < 0$. Depending on the g_h sign, $\mathbf{B}_{N,h}$ can increase or reduce the hole Zeeman splitting induced by an external magnetic field. Therefore, it changes the spin-flip Raman shift and can be detected experimentally by SFRS. For example, we have demonstrated that for (In,Ga)As/GaAs quantum dots.[69]

In order to examine the DNP in $(PEA)_2PbI_4$, we apply the SFRS technique in close-to-Faraday geometry (θ = 10°). The signal is detected in σ^- circular polarization, while the excitation polarization was set to either σ^+ or σ^-. As shown in Figure 4a the shift of the hole spin-flip line is larger in the $\sigma^-\sigma^-$ configuration (we label the shift as E_h^- shown by the blue arrow) than in the $\sigma^+\sigma^-$ configuration (E_h^+, the red arrow). Their difference scales with twice the Overhauser field which thus can be extracted from the relation

$$\Delta E_{N,h} = |E_h^+| - |E_h^-| = 2|g_{h,c}|\mu_B B_{N,h} \quad (5)$$

as sketched in Figure 4f. The difference $\Delta E_{N,h} = |E_h^+| - |E_h^-| = -1.6\ \mu$eV measured at P = 5.1 W cm^{-2} corresponds to $B_{N,\,h} = -0.11$ T calculated using $|g_{h,c}| = 0.13$. The negative sign of $B_{N,\,h}$ means that $g_{h,c} < 0$, see Equation (4).

The nuclear-induced shift can be seen even more clearly in the double spin-flip line $E_{e\,+\,h}$, as for it the background contribution of the scattered laser light is strongly reduced, see Figure 4b. Note that the DNP shift is absent for the electron Zeeman splitting, as the E_e shift is the same for the $\sigma^-\sigma^-$ and $\sigma^+\sigma^-$ configurations. However, the shift of the E_{e+h} line from E_e varies. For the used excitation density of 13.5 W cm^{-2} the energy splitting of these lines amounts to $\Delta E_{N,h} = -5.5$ μeV and, therefore, to $B_{N,h} = -0.36$ T.

The excitation density dependences of $\Delta E_N(P)$ and $B_N(P)$ for electrons and holes are shown in Figure 4c. As already noted, any effect on the electrons is absent, reflecting the expected weak hyperfine interaction in the 2D $(PEA)_2PbI_4$ perovskite. The energy splitting is pronounced for holes, for which the $\Delta E_{N,h}$ value increases up to −8.7 μeV, which corresponds to $B_{N,h} = -0.6$ T at P = 10.5 W cm^{-2}. For a further excitation density increase the energy splitting becomes weaker, which we assign to heating of the nuclear spin system.

The results of this section show that the SFRS technique is a valuable tool for providing insight into the central spin problem of a carrier spin placed in a nuclear spin bath in 2D perovskite materials and also for studying perovskite bulk crystals and nanocrystals.

2.7. Discussion

Let us discuss the mechanisms that can be responsible for the observed spin-flip processes. Recently a detailed theoretical analysis of the spin-flip Raman scattering processes involving excitons and resident charge carriers in perovskite semiconductors was published.[66] The model considerations were made for bulk perovskites with cubic symmetry. Three mechanisms for the observation of carrier spin-flips were suggested that can explain both the single and double spin-flip processes. The first mechanism is the resonant excitation of a localized exciton, followed by its exchange interaction with a resident electron and/or hole. The second mechanism involves a biexciton as an intermediate state of the SFRS. In this case, spin-flip shifts by the energies of E_{e+h} and $E_{e+h}/2$ are expected, but the process with $E_{e\text{-}h}$ is forbidden. We observe, however, in the experiment the $E_{e\text{-}h}$ process, which allows us to exclude the biexciton scenario. The third mechanism is the direct excitation of propagating exciton–polaritons, their scattering on resident carriers, and the conversion of the polaritons into secondary photons at the sample boundary. In 2D perovskites the semiconductor layers are electronically decoupled from each other which prevents exciton–polariton motion along the c-axis. Therefore, we suggest that the exciton–polariton mechanism can be neglected for them.

Our experimental results on the spectral dependence of the SFRS intensity clearly show the exciton involvement. In turn, the Raman shift values and their anisotropy allow us to refer them to resident carriers, which interact with the exciton acting as a mediator of the SFRS. The considerations of ref. [66] predict pronounced polarization dependencies for the carrier spin-flip lines. So far, the reason why such dependencies are not observed here is unclear, see Figure S1, Supporting Information. Future analysis accounting for the reduced symmetry and mixing of the bright exciton states in 2D perovskites might clarify this property. Note that the 2D perovskites are similar to 2D CdSe colloidal nanoplatelets, but for the nanoplatelets we do observe pronounced polarization dependences of the spin-flip lines.[55] The SFRS theory for the CdSe nanoplatelets is presented in ref. [67]. Here, the violation of polarization selection rules caused by the in-plane anisotropy of the nanoplatelets, which induces exciton mixing and splitting, and by the finite Zeeman splitting of the intermediate state were analyzed.

We have measured the exciton g-factor in $(PEA)_2PbI_4$ of $g_{X,c} = +1.6$ from the exciton Zeeman splitting in magneto-reflectivity, see Figure 1c. It is in agreement with reported experimental data for 2D perovskite excitons measured in pulsed magnetic fields up to 60 T, where either magneto-transmission or magneto-reflectivity were used. The exciton g-factor of about 1.2 was measured for $(PEA)_2PbI_4$.[38] For the similar 2D perovskite

© 2023 The Authors. Small published by Wiley-VCH GmbH

16136829, 2023, 32, Downloaded from https://onlinelibrary.wiley.com/doi/10.1002/smll.202300988 by Technische Universitaet Dortmund, Wiley Online Library on [07/02/2025]. See the Terms and Conditions (https://onlinelibrary.wiley.com/terms-and-conditions) on Wiley Online Library for rules of use; OA articles are governed by the applicable Creative Commons License

$(C_6H_{13}NH_3)_2PbI_4$ it amounts to about 1.5[70] and +1.80.[36] For $(C_{10}H_{21}NH_3)_2PbI_4$ it is +1.42,[37] and for the halogen substitution for Br in $(C_4H_9NH_3)_2PbBr_4$ the *g*-factor is +1.2.[24]

Another type of spin-flip Raman scattering process was observed in the $(C_4H_9NH_3)_2PbBr_4$ 2D perovskite.[25] These experiments were performed at zero magnetic field, where the Raman shift by the large value of 25–28 meV arises from the flip of the exciton spin between the optically allowed Γ_5^- state and optically forbidden Γ_2^- state. This shift originates from the exchange splitting of the excitons and is not related to their Zeeman splitting.

3. Conclusions

We have investigated the spin properties of 2D $(PEA)_2PbI_4$ perovskites using spin-flip Raman scattering. We have found spin-flip signals from resident electrons and holes, as well as their combinations. This has allowed us to measure the Landé factors and their anisotropy. The anisotropy of the electron and hole *g*-factors is complementary, so that their sum corresponding to the bright exciton *g*-factor remains isotropic. Also, hyperfine hole-nuclei interaction is demonstrated in 2D perovskites by means of the dynamic nuclear polarization. Due to the small *g*-factor of the hole, we were able to achieve an Overhauser field value of $B_{N,h} = 0.6$ T. The direction of $\mathbf{B}_{N,h}$ allows us to unambiguously determine the negative sign of the hole *g*-factor. We are convinced that similar effects as those observed can manifest themselves in the large class of 2D lead halide perovskites with different numbers of layers, as well as in perovskites with various organic cations.

4. Experimental Section

*Samples:*Ruddlesden–Popper type 2D $(PEA)_2PbI_4$ perovskites that consist of a stack of monolayers formed by corner-shared PbI_6 octahedra are studied. The monolayers were separated by van der Waals-bonded pairs of PEA [phenethylammonium $(C_6H_5)C_2H_4NH_3$] molecules. Details of the synthesis are given in the Section S1, Supporting Information, and in ref. [48]. Due to the quantum confinement of electrons and holes the band gap energy of $(PEA)_2PbI_4$ is 2.608 eV at $T = 2$ K.[38] This value considerably exceeded the band gap energy of $APbI_3$ lead iodine archetype bulk crystals with $E_g = 1.5$–1.7 eV, where $A = Cs^+$, MA^+, or FA^+. The reduced dimensionality and the dielectric enhancement effect, provided by the contrast in dielectric constants between the perovskite monolayers and the PEA, strongly increased the exciton binding energy in $(PEA)_2PbI_4$ to 260 meV[38,42] in comparison to 16 meV in bulk $MAPbI_3$ perovskite.[56]

*SFRS Spectroscopy:*The SFRS technique enabled one to directly measure the Zeeman splitting of the electron and hole spins from the spectral shift of the scattered light from the laser photon energy. Resonant excitation of the exciton strongly increased the SFRS signals, allowing one to measure resident electrons and holes interacting with an exciton. For optical excitation a tunable single-frequency continuous wave Ti:Sapphire laser (Matisse DS) equipped with a MixTrain module from SIRAH was used. The emitted photon energy was tuned around 530 nm (spectral range 2.33–2.36 eV), provided by the sum frequency of the Ti:Sapphire laser operating around 720 nm and a fiber laser emitting at 1950 nm. The actual wavelength was measured and monitored by a fiber-coupled high-resolution wavemeter (HighFinesse WSU). The laser power after the MixTrain module was generally set to 0.7 mW. The diameter of the laser spot on the sample was 180 µm resulting in an excitation density of $P = 2.75$ W cm^{-2}, if not specified otherwise. The linear or circular polarizations of the laser beam and the Raman signal were set and analyzed by combinations of $\lambda/2$ or $\lambda/4$ wave plates and a Glan–Thompson prism, positioned in the excitation and detection paths. The linear polarizations were denoted as V (vertical) and H (horizontal), and the circular polarizations as σ^+ and σ^-.

The Raman signals were measured in backscattering geometry. The light scattered from the sample was dispersed by a 1 m double monochromator (Yobin-Yvon U1000) equipped with a Peltier-cooled GaAs photomultiplier providing a spectral resolution of 0.8 µeV. For the studied sample this allowed to measure *g*-factors with an accuracy of 0.05. To protect the photomultiplier from the highly intense laser light, a neutral density filter was placed in the detection path while recording the laser. The SFRS measurements were performed at the low temperature of $T = 1.6$ K with the sample immersed in pumped liquid helium. Magnetic fields up to 10 T generated by a superconducting split-coil solenoid were applied. In Figure 2a the used experimental geometries are shown. The sample axes *a* and *b* are in-plane, while the *c*-axis is out-of-plane. In the Faraday geometry, the magnetic field is parallel to the light wave vector *k* and to the *c*-axis ($\mathbf{B}_F \| \mathbf{k}$, $\mathbf{B}_F \| c$ and $\theta = 0°$). In the Voigt geometry the field is perpendicular to these vectors ($\mathbf{B}_V \perp \mathbf{k}$, $\mathbf{B}_V \| (a, b)$ and $\theta = 90°$). In the experiments the orientations of the *a*- and *b*-axes were not distinguished and therefore the measured values were averaged over their random orientations, while the differences between the two axes were not expected to be large. The angle θ between the *c*-axis and the magnetic field specified the tilt of the field directions as shown in the bottom diagram, where $\mathbf{k} \| \mathbf{B}$ was kept.

*Photoluminescence:*Nonresonant continuous wave excitation with the photon energy of 2.412 eV and an excitation density of $P = 10.8$ W cm^{-2} was used for the PL measurements performed at $T = 1.6$ K. The PL was detected by the same 1 m double monochromator (U1000) and GaAs photomultiplier, as in the SFRS measurements.

*Time-Resolved Photoluminescence:*For the TRPL measurements, a pulsed excitation laser was used (pulse duration of 10 ns, pulse repetition rate of 800 Hz, photon energy of 3.493 eV, and excitation density of $P = 3$ W cm^{-2}). The PL was detected again with the Peltier-cooled GaAs photomultiplier coupled to the U1000. The time resolution of the recombination dynamics was provided by a time-of-flight electronic board (Fast ComTec MCS6A), which had a nominal time resolution of 100 ps. In the experiment the time resolution of 10 ns was limited by the laser pulse duration.

Supporting Information

Supporting Information is available from the Wiley Online Library or from the author.

Acknowledgements

The authors are thankful to A. V. Rodina, E. L. Ivchenko, M. O. Nestoklon, M. M. Glazov, and I. V. Kalitukha for fruitful discussions. The authors acknowledge the financial support by the Deutsche Forschungsgemeinschaft in the frame of the Priority Programme SPP 2196 (Project YA 65/26-1) and the International Collaboration Research Center TRR160 (Projects A1 and B2). The work of O.H. and M.V.K. was financially supported by the Swiss National Science Foundation (grant agreement 186406, funded in conjunction with SPP2196 through DFG-SNSF bilateral program) and by the ETH Zürich through the ETH+ Project SynMatLab: Laboratory for Multiscale Materials Synthesis.

Open access funding enabled and organized by Projekt DEAL.

Conflict of Interest

The authors declare no conflict of interest.

© 2023 The Authors. Small published by Wiley-VCH GmbH

16136829, 2023, 32, Downloaded from https://onlinelibrary.wiley.com/doi/10.1002/smll.202300988 by Technische Universitaet Dortmund, Wiley Online Library on [07/02/2025]. See the Terms and Conditions (https://onlinelibrary.wiley.com/terms-and-conditions) on Wiley Online Library for rules of use; OA articles are governed by the applicable Creative Commons License

Data Availability Statement

The data that support the findings of this study are available from the corresponding author upon reasonable request.

Keywords

2D perovskites, dynamic nuclear polarization,g-factor, hyperfine interaction, spin-flip Raman scattering, spintronics

Received: February 3, 2023
Revised: March 14, 2023
Published online: April 17, 2023

[1] *Halide Perovskites for Photonics*, (Eds.: A. Vinattieri, G. Giorgi), AIP Publishing, Melville, NY **2021**.
[2] *Hybrid Organic Inorganic Perovskite Applications, in Hybrid Organic Inorganic Perovskites: Physical Properties and Applications*, Vol. *4*, (Eds.: Z. V. Vardeny, M. C. Beard), World Scientific, Singapore **2022**.
[3] A. K. Jena, A. Kulkarni, T. Miyasaka, *Chem. Rev.* **2019**, *5*, 3036.
[4] C. Hansell, L. Fleet, M. Lee, E. Couderc, G. Tregnago, L. Martiradonna, O. Bubnova, O. Graydon, J. P. Kraack, B. Liu, M. Citroni, G. Graziano, A. Stoddart, Perovskites for optoelectronics, https://www.nature.com/collections/fnnxcznnbb/content/reviews (Accessed: September 2019).
[5] L. Mao, C. C. Stoumpos, M. G. Kanatzidis, *J. Am. Chem. Soc.* **2018**, *141*, 1171.
[6] J.-C. Blancon, J. Even, C. C. Stoumpos, M. G. Kanatzidis, A. D. Mohite, *Nat. Nanotechnol.* **2020**, *15*, 969.
[7] R. L. Z. Hoye, J. Hidalgo, R. A. Jagt, J.-P. Correa-Baena, T. Fix, J. L. MacManus-Driscoll, *Adv. Energy Mater.* **2022**, *12*, 02100499.
[8] N. Wang, L. Cheng, R. Ge, S. Zhang, Y. Miao, W. Zou, C. Yi, Y. Sun, Y. Cao, R. Yang, Y. Wei, Q. Guo, Y. Ke, M. Yu, Y. Jin, Y. Liu, Q. Ding, D. Di, L. Yang, G. Xing, H. Tian, C. Jin, F. Gao, R. H. Friend, J. Wang, W. Huang, *Nat. Photonics* **2020**, *10*, 699.
[9] K. Łempicka-Mirek, M. Król, H. Sigurdsson, A. Wincukiewicz, P. Morawiak, R. Mazur, M. Muszyński, W. Piecek, P. Kula, T. Stefaniuk, M. Kamińska, L. De Marco, P. G. Lagoudakis, D. Ballarini, D. Sanvitto, J. Szczytko, B. Pietka, *Sci. Adv.* **2022**, *8*, eabq7533.
[10] X. Zhang, R. Munir, Z. Xu, Y. Liu, H. Tsai, W. Nie, J. Li, T. Niu, D.-M. Smilgies, M. G. Kanatzidis, A. D. Mohite, K. Zhao, A. Amassian, S. F. Liu, *Adv. Mater.* **2018**, *30*, 1707166.
[11] P. Cheng, Z. Xu, J. Li, Y. Liu, Y. Fan, L. Yu, D.-M. Smilgies, C. Müller, K. Zhao, S. F. Liu, *ACS Energy Lett.* **2018**, *3*, 1975.
[12] S. Sidhik, Y. Wang, W. Li, H. Zhang, X. Zhong, A. Agrawal, I. Hadar, I. Spanopoulos, A. Mishra, B. Traoré, M. H. K. Samani, C. Katan, A. B. Marciel, J.-C. Blancon, J. Even, A. Kahn, M. G. Kanatzidis, A. D. Mohite, *Cell Rep. Phys. Sci.* **2021**, *2*, 100601.
[13] a) E. A. Muljarov, S. G. Tikhodeev, N. A. Gippius, T. Ishihara, *Phys. Rev. B* **1995**, *51*, 14370; b) L. V. Kulik, V. D. Kulakovskii, M. Bayer, A. Forchel, N. A. Gippius, S. G. Tikhodeev, *Phys. Rev. B* **1996**, *54*, 2335.
[14] J.-C. Blancon, A. V. Stier, H. Tsai, W. Nie, C. C. Stoumpos, B. Traoré, L. Pedesseau, M. Kepenekian, F. Katsutani, G. T. Noe, J. Kono, S. Tretiak, S. A. Crooker, C. Katan, M. G. Kanatzidis, J. J. Crochet, J. Even, A. D. Mohite, *Nat. Commun.* **2018**, *9*, 2254.
[15] T. Ishihara, J. Takahashi, T. Goto, *Solid State Commun.* **1989**, *69*, 933.
[16] T. Ishihara, J. Takahashi, T. Goto, *Phys. Rev. B* **1990**, *42*, 11099.
[17] G. Wang, A. Chernikov, M. M. Glazov, T. F. Heinz, X. Marie, T. Amand, B. Urbaszek, *Rev. Mod. Phys.* **2018**, *90*, 021001.
[18] J. Even, L. Pedesseau, C. Katan, M- Kepenekian, J.-S. Lauret, D. Sapori, E. Deleporte, *J. Phys. Chem.* **2015**, *119*, 10161.
[19] C. Katan, N. Mercier, J. Even, *Chem. Rev.* **2019**, *119*, 3140.
[20] Z. Yu, *Sci. Rep.* **2016**, *6*, 28576.
[21] E. Kirstein, D. R. Yakovlev, M. M. Glazov, E. Evers, E. A. Zhukov, V. V. Belykh, N. E. Kopteva, D. Kudlacik, O. Nazarenko, D. N. Dirin, M. V. Kovalenko, M. Bayer, *Adv. Mater.* **2022**, *34*, 2105263.
[22] E. Kirstein, D. R. Yakovlev, M. M. Glazov, E. A. Zhukov, D. Kudlacik, I. V. Kalitukha, V. F. Sapega, G. S. Dimitriev, M. A. Semina, M. O. Nestoklon, E. L. Ivchenko, N. E. Kopteva, D. N. Dirin, O. Nazarenko, M. V. Kovalenko, A. Baumann, J. Höcker, V. Dyakonov, M. Bayer, *Nat. Commun.* **2022**, *13*, 3062.
[23] *Spin Response of Hybrid Organic Inorganic Perovskites, in Hybrid Organic Inorganic Perovskites: Physical Properties and Applications*, Vol. *3*, (Eds.: Z. V. Vardeny, M. C. Beard), World Scientific, Singapore **2022**.
[24] K. Tanaka, T. Takahashi, T. Kondo, K. Umeda, K. Ema, T. Umebayashi, K. Asai, K. Uchida, N. Miura, *Jap. J. Appl. Phys.* **2005**, *44*, 5923.
[25] K. Ema, K. Umeda, M. Toda, C. Yajima, Y. Arai, H. Kunugita, D. Wolverson, J. J. Davies, *Phys. Rev. B* **2006**, *73*, 241310(R).
[26] M. Gramlich, M. W. Swift, C. Lampe, J. L. Lyons, M. Döblinger, Al. L. Efros, P. C. Sercel, A. S. Urban, *Adv. Sci.* **2022**, *9*, 2103013.
[27] D. Giovanni, H. Ma, J. Chua, M. Grätzel, R. Ramesh, S. Mhaisalkar, N. Mathews, T. C. Sum, *Nano Lett.* **2015**, *15*, 1553.
[28] M. O. Nestoklon, S. V. Goupalov, R. I. Dzhioev, O. S. Ken, V. L. Korenev, Yu. G. Kusrayev, V. F. Sapega, C. de Weerd, L. Gomez, T. Gregorkiewicz, J. Lin, K. Suenaga, Y. Fujiwara, L. B. Matyushkin, I. N. Yassievich, *Phys. Rev. B* **2018**, *97*, 235304.
[29] R. Wang, S. Hu, X. Yang, X. Yan, H. Li, C. Sheng, *J. Mater. Chem. C* **2018**, *6*, 2989.
[30] J. Wang, C. Zhang, H. Liu, R. McLaughlin, Y. Zhai, S. R. Vardeny, X. Liu, S. McGill, D. Semenov, H. Guo, R. Tsuchikawa, V. V. Deshpande, D. Sun, Z. V. Vardeny, *Nat. Commun.* **2019**, *10*, 129.
[31] C. Zhang, D. Sun, C-X. Sheng, Y. X. Zhai, K. Mielczarek, A. Zakhidov, Z. V. Vardeny, *Nat. Phys.* **2015**, *11*, 427.
[32] D. Canneson, E. V. Shornikova, D. R. Yakovlev, T. Rogge, A. A. Mitioglu, M. V. Ballottin, P. C. M. Christianen, E. Lhuillier, M. Bayer, L. Biadala, *Nano Lett.* **2017**, *17*, 6177.
[33] C. Zhang, D. Sun, Z.-G. Yu, C.-X. Sheng, S. McGill, D. Semenov, Z. V. Vardeny, *Phys. Rev. B* **2018**, *97*, 134412.
[34] P. Odenthal, W. Talmadge, N. Gundlach, R. Wang, C. Zhang, D. Sun, Z.-G. Yu, Z. V. Vardeny, Y. S. Li, *Nat. Phys.* **2017**, *13*, 894.
[35] V. V. Belykh, D. R. Yakovlev, M. M. Glazov, P. S. Grigoryev, M. Hussain, J. Rautert, D. N. Dirin, M. V. Kovalenko, M. Bayer, *Nat. Commun.* **2019**, *10*, 673.
[36] T. Kataoka, T. Kondo, R. Ito, S. Sasaki, K. Uchida, N. Miura, *Phys. Rev. B* **1993**, *47*, 2010.
[37] M. Hirasawa, T. Ishihara, T. Goto, S. Sasaki, K. Uchida, N. Miura, *Solid State Commun.* **1993**, *86*, 479.
[38] M. Dyksik, H. Duim, X. Zhu, Z. Yang, M. Gen, Y. Kohama, S. Adjokatse, D. K. Maude, M. A. Loi, D. A. Egger, M. Baranowski, P. Plochocka, *ACS Energy Lett.* **2020**, *5*, 3609.
[39] M. Dyksik, H. Duim, D. K. Maude, M. Baranowski, M. A. Loi, P. Plochocka, *Sci. Adv.* **2021**, *7*, eabk0904.
[40] T. T. H. Do, A. G. del Águila, D. Zhang, J. Xing, S. Liu, M. A. Prosnikov, W. Gao, K. Chang, P. C. M. Christianen, Q. Xiong, *Nano Lett.* **2020**, *20*, 5141.
[41] A. Surrente, M. Baranowski, P. Plochocka, *Appl. Phys. Lett.* **2021**, *118*, 170501.
[42] M. Baranowski, M. Dyksik, P. Plochocka, *Sci. Radices* **2022**, *1*, 3.
[43] D. Giovanni, W. K. Chong, Y. Y. F. Liu, H. A. Dewi, T. Yin, Y. Lekina, Z. X. Shen, N. Mathews, C. K. Gan, T. C. Sum, *Adv. Sci.* **2018**, *5*, 1800664.
[44] X. Pan, H. Liu, U. Huynh, Z. V. Vardeny, *J. Chem. Phys.* **2020**, *152*, 044714.

© 2023 The Authors. Small published by Wiley-VCH GmbH

16136829, 2023, 32, Downloaded from https://onlinelibrary.wiley.com/doi/10.1002/smll.202300988 by Technische Universitaet Dortmund, Wiley Online Library on [07/02/2025]. See the Terms and Conditions (https://onlinelibrary.wiley.com/terms-and-conditions) on Wiley Online Library for rules of use; OA articles are governed by the applicable Creative Commons License

[45] X. Chen, H. Lu, K. Wang, Y. Zhai, V. Lunin, P. C. Sercel, M. C. Beard, *J. ACS* **2021**, *143*, 19438.
[46] S. A. Bourelle, R. Shivanna, F. V. A. Camargo, S. Ghosh, A. J. Gillett, S. P. Senanayak, S. Feldmann, L. Eyre, A. Ashoka, T. W. J. van de Goor, H. Abolins, T. Winkler, G. Cerullo, R. H. Friend, F. Deschler, *Nano Lett.* **2020**, *20*, 5678.
[47] S. A. Bourelle, F. V. A. Camargo, S. Ghosh, T. Neumann, T. W. J. van de Goor, R. Shivanna, T. Winkler, G. Cerullo, F. Deschler, *Nat. Commun.* **2022**, *13*, 3320.
[48] E. Kirstein, E. A. Zhukov, D. R. Yakovlev, N. E. Kopteva, C. Harkort, D. Kudlacik, O. Hordiichuk, M. V. Kovalenko, M. Bayer, *Nano Lett.* **2023**, *23*, 205.
[49] D. G. Thomas, J. J. Hopfield, *Phys. Rev.* **1968**, *175*, 1021.
[50] H. G. Häfele, in *Landau Level Spectroscopy*, Vol. *27*, (Eds.: G. Landwehr, E. I. Rashba), Elsevier, Amsterdam **1991**, pp. 208–275.
[51] V. F. Sapega, T. Ruf, M. Cardona, K. Ploog, E. L. Ivchenko, D. N. Mirlin, *Phys. Rev. B* **1994**, *50*, 2510.
[52] A. A. Sirenko, T. Ruf, M. Cardona, D. R. Yakovlev, W. Ossau, A. Waag, G. Landwehr, *Phys. Rev. B* **1997**, *56*, 2114.
[53] J. Debus, D. Dunker, V. F. Sapega, D. R. Yakovlev, G. Karczewski, T. Wojtowicz, J. Kossut, M. Bayer, *Phys. Rev. B* **2013**, *87*, 205316.
[54] J. Debus, V. F. Sapega, D. Dunker, D. R. Yakovlev, D. Reuter, A. D. Wieck, M. Bayer, *Phys. Rev. B* **2014**, *90*, 235404.
[55] D. Kudlacik, V. F. Sapega, D. R. Yakovlev, I. V. Kalitukha, E. V. Shornikova, A. V. Rodina, E. L. Ivchenko, G. S. Dimitriev, M. Nasilowski, B. Dubertret, M. Bayer, *Nano Lett.* **2020**, *20*, 517.
[56] K. Galkowski, A. Mitioglu, A. Miyata, P. Plochocka, O. Portugall, G. E. Eperon, J. Tse-Wei Wang, T. Stergiopoulos, S. D. Stranks, H. J. Snaith, R. J. Nicholas, *Energy Environ. Sci.* **2016**, *9*, 962.
[57] K. Posmyk, N. Zawadzka, M. Dyksik, A. Surrente, D. K. Maude, T. Kazimierczuk, A. Babinski, M. R. Molas, W. Paritmongkol, M. Maczka, W. A. Tisdale, P. Plochocka, M. Baranowski, *J. Phys. Chem. Lett.* **2022**, *13*, 4463.
[58] T. Thu Ha Do, A. Granados del Águila, J. Xing, S. Liu, Q. Xiong, *J. Chem. Phys.* **2020**, *153*, 064705.
[59] S. Kahmann, H. Duim, H.-H. Fang, M. Dyksik, S. Adjokatse, M. Rivera Medina, M. Pitaro, P. Plochocka, M. A. Loi, *Adv. Funct. Mater.* **2021**, *31*, 2103778.
[60] H.-H. Fang, J. Yang, S. Adjokatse, E. Tekelenburg, M. E. Kamminga, H. Duim, J. Ye, G. R. Blake, J. Even, M. A. Loi, *Adv. Funct. Mater.* **2020**, *30*, 1907979.
[61] E. Kirstein, D. R. Yakovlev, E. A. Zhukov, J. Höcker, V. Dyakonov, M. Bayer, *ACS Photonics* **2022**, *9*, 1375.
[62] T. Neumann, S. Feldmann, P. Moser, A. Delhomme, J. Zerhoch, T. van de Goor, S. Wang, M. Dyksik, T. Winkler, J. J. Finley, P. Plochocka, M. S. Brandt, C. Faugeras, A. V. Stier, F. Deschler, *Nat. Commun.* **2021**, *12*, 3489.
[63] J. F. Scott, T. C. Damen, *Phys. Rev. Lett.* **1972**, *29*, 107.
[64] Y. Oka, M. Cardona, *Phys. Rev. B* **1981**, *293*, 4129.
[65] E. N. Economou, J. Ruvalds, K. L. Ngai, *Phys. Rev. Lett.* **1972**, *29*, 110.
[66] A. V. Rodina, E. L. Ivchenko, *Phys. Rev. B* **2022**, *106*, 245202.
[67] A. V. Rodina, E. L. Ivchenko, *Phys. Rev. B* **2020**, *102*, 235432.
[68] *Optical Orientation*, (Eds.: F. Meier, B. P. Zakharchenya), Elsevier, New York **1984**.
[69] J. Debus, D. Kudlacik, V. F. Sapega, D. Dunker, P. Bohn, F. Paßmann, D. Braukmann, J. Rautert, D. R. Yakovlev, D. Reuter, A. D. Wieck, M. Bayer, *Phys. Rev. B* **2015**, *92*, 195421.
[70] M. Baranowski, S. J. Zelewski, M. Kepenekian, B. Traore, J. M. Urban, A. Surrente, K. Galkowski, D. K. Maude, A. Kuc, E. P. Booker, R. Kudrawiec, S. D. Stranks, P. Plochocka, *ACS Energy Lett.* **2019**, *4*, 2386.

© 2023 The Authors. Small published by Wiley-VCH GmbH

16136829, 2023, 32, Downloaded from https://onlinelibrary.wiley.com/doi/10.1002/smll.202300988 by Technische Universitaet Dortmund, Wiley Online Library on [07/02/2025]. See the Terms and Conditions (https://onlinelibrary.wiley.com/terms-and-conditions) on Wiley Online Library for rules of use; OA articles are governed by the applicable Creative Commons License